Localizing dexterous surgical tools in X-ray for image-based navigation*

Cong Gao
1,2,*, Mathias Unberath^{1,2,*}, Russell Taylor^{1,2}, and Mehran Armand^{2,3,4}

Department of Computer Science, Johns Hopkins University
Laboratory for Computational Sensing and Robotics, Johns Hopkins University
Johns Hopkins University Applied Physics Laboratory
Department of Orthopaedic Surgery, Johns Hopkins Hospital
Joint first authors.
cgao11@jhu.edu

1 Purpose

Continuum dexterous manipulators (CDMs), commonly referred to as snakelike robots, have demonstrated great premise for minimmally-invasive procedures [11,4]. Recent innovations have made CDMs appropriate for use in orthopedic surgery [5,8,1]. One key challenge of using CDMs is performing precise intra-operative control guided by a pre-operative patient-specific plan, conceived based on 3D imaging and potentially bio-mechanical analysis. To this end, the calibration loop of robot base to end-effector to patient anatomy must be closed. and an accurate kinematic deformation estimation of the CDM is required. X-ray image based surgical tool navigation has received increasing interest since it is fast and supplies accurate images of deep seated structures. Typically, recovering the 6 degree of freedom (DOF) rigid pose and deformation of tools with respect to the X-ray camera can be accurately achieved through intensity-based 2D/3D registration of 3D images or models to 2D X-rays [7]. However, it is well known that the capture range of image-based 2D/3D registration is inconveniently small suggesting that automatic and robust initialization strategies are of critical importance. Consequently, this manuscript describes a first step towards leveraging semantic information of the imaged object to initialize 2D/3D registration within the capture range of image-based registration by performing concurrent segmentation and localization of the CDM in X-ray images.

2 Methods

We seek to train a convolutional neural network (ConvNet) to localize CDMs in X-ray images. The CDM developed by our group considered here is fabricated using Nitinol. Its outer diameter is 6 mm and it includes an instrument

 $^{^\}star$ This work was supported in part by NIH R01 EB023939 and Johns Hopkins University internal funding sources.

channel with a diameter of 4 mm. A set of 26 alternating notches on the body of the CDM allow for single-plane bending [5,8]. Due to the unavailability of annotated X-ray images to train ConvNets, we rely on DeepDRR [10], a framework for physics-based rendering of digitally reconstructed radiographs (DRRs, i.e. synthetic fluoroscopic images) from 3D CT. DeepDRR accurately accounts for energy- and material-dependence of X-ray attenuation, scattering, and noise. Recent work [10.3] demonstrated that ConvNets trained on DeepDRRs generalize to clinically acquired X-ray images without re-training, motivating its use for the application proposed here. The simulation of the CDM mainly consists of two parts: 1) body and base of the CDM plus an extended shaft; and 2) inserted tool and drill. Following previous work on kinematic modeling of this CDM [9], we assume that the joint angle changes smoothly from one joint to the next. Angles are parameterized as cubic spline of n=5 equally distributed control points, τ_i , along the central axis of the CDM. The rigid pose of the CDM relative to X-ray camera is represented by translation and rotation in x, y, and z axes, defining the total parameter space as $\theta = \{t_x, t_y, t_z, r_x, r_y, r_z, c\}, (c = \{\tau_1, ..., \tau_n\}).$ Given a 3D CT of the lower torso, we manually define a rigid transformation such that the CDM model is enclosed in the femur, simulating applications in core decompression and fracture repair [1,2]. DeepDRR uses voxel representation, so the CDM surface model is voxelized with high resolution to preserve details of the notches. At positions where the CT volume exhibits overlap with the CDM, CT values are omitted to model drilling. From the above volumes and coordinate transforms, we use DeepDRR to generate 1) realistic X-ray images, 2) 2D segmentation masks of the CDM end-effector, and 3) 2D locations of two key landmarks. Our segmentation target region covers the 26 alternating notches which discerns the CDM from other surgical tools. The two landmarks are defined as 1) the middle of the 2 conjunction points between the first notch and the base and 2) the center of the distal plane of the last notch, i.e. start and end point of CDM centerline. The simulated X-rays have 512×512 pixels with an isotropic pixel size of (0.62 mm)². DRRs are converted to line-integral domain to decrease the dynamic range and then normalized to [-1, 1]. Landmark coordinates are transformed to belief maps expressed as Gaussian distributions $(\sigma = 5 \text{ pixels})$ around the true location. Data generation was done as follows: A total of 5 lower-limbs CTs ($512 \times 512 \times 2590$ voxel, $0.85 \text{ mm}^3/\text{voxel}$) were included in the experiment and centered around the pelvis. The CDM volume was manually aligned with the left/right femur to mimic our clinical usecase. Then, CDM shapes and rigid X-ray source and volume poses were sampled randomly: Source-to-detector distance was fixed to 1200 mm while source-to-isocenter distance was \in [400 mm, 500 mm]. Source rotation in LAO/RAO was \in [0°, 360°] and in CRAN/CUAD \in [75°, 105°]. Volume translation was \in [-20, 20] mm in all axes. CDM shapes were defined by randomly sampling control point angles $\in [-7.9^{\circ}, 7.9^{\circ}]$. We sampled a total of 1,000 random configurations per femoral head (10,000 total) to render synthetic images. CTs were split 4:1 into training:testing, and within the training dataset 10:1 into training:validation. We also manually annotated 87 X-ray images of a real CDM drilling in femoral bone

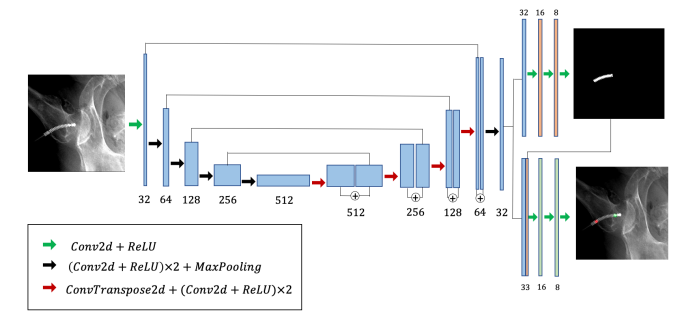


Fig. 1. Network architecture used for concurrent segmentation and landmark detection.

specimens for quantitative evaluation on cadaveric data.

Inspired by the work of [6], we design a ConvNet-based auto-encoder like architecture with skip connections, and split the connection from the last feature layer to perform two tasks concurrently, i.e. segmentation and landmark detection. Fig. 1 illustrates the ConvNet architecture used here. In the decoder, we repeat the connection of 2D convolutional layer and maxpooling layer four times to abstract a feature representation with 512 channels. In the decoder part, we concatenate the upsampled features and features from the same level in the encoding stage. The final decoded 32 channel feature layer is shared across the segmentation path and the localization path. The final output of the segmentation mask is backward concatenated with this shared feature to boost the localization task. We chose Dice loss to train the segmentation task and the standard L_2 loss for the localization task. Learning rate was initialized with 0.001 and decayed by 0.1 every 10 epochs.

3 Results

The segmentation accuracy is computed as the Dice score of mask prediction. Landmark detection accuracy is reported as the L_2 distance in millimeters. We first evaluated the network on the synthetic dataset where exact groundtruth was known. The mean Dice score was 0.996 ± 0.001 and the mean L_2 distance was 0.365 ± 0.345 mm. On the manually annotated 87 ex vivo X-ray images, the network achieved a mean Dice score of 0.915 ± 0.063 and mean L_2 distance of 2.54 ± 0.95 mm. The cadaveric data contained configurations never seen during training (i. e. tool completely outside bone) that induced poor performance of our network, as reflected in the high standard deviations for the cadaveric dataset. Representative results are shown in Fig. 2.

4 Conclusions

We presented a learning-based strategy to simultaneously localize and segment dexterous surgical tools in X-ray images. Our results on synthetic and *ex vivo*

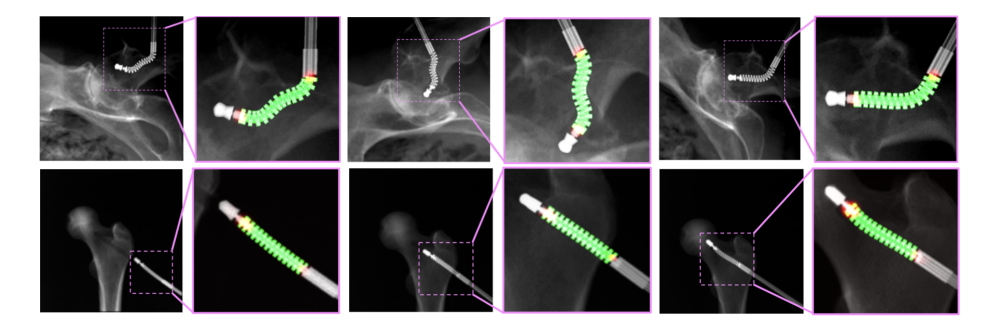


Fig. 2. Representative examples of segmentation and landmark detection performance on synthetic (upper row) and real *ex vivo* data (lower row). The predicted segmentation and landmarks are shown as green and red overlay, respectively.

data are promising and encourage training of our ConvNet on a more exhaustive dataset. We currently investigate how these results translate to other real data and investigate methods to use semantic information extracted by the proposed network to reliably and robustly initialize image-based 2D/3D registration.

References

- Alambeigi, F., et al.: A curved-drilling approach in core decompression of the femoral head osteonecrosis using a continuum manipulator. IEEE Robot Autom Lett 2(3), 1480–1487 (2017)
- Alambeigi, F., et al.: Inroads toward robot-assisted internal fixation of bone fractures using a bendable medical screw and the curved drilling technique. In: IEEE Conf on Biorob. pp. 595–600. IEEE (2018)
- 3. Bier, B., Unberath, M., et al.: X-ray-transform invariant anatomical landmark detection for pelvic trauma surgery. In: Proc MICCAI (2018)
- 4. Burgner-Kahrs, J., et al.: Continuum robots for medical applications: A survey. IEEE Trans Robot **31**(6), 1261–1280 (2015)
- 5. Kutzer, M.D., et al.: Design of a new cable-driven manipulator with a large open lumen: Preliminary applications in the minimally-invasive removal of osteolysis. In: Proc ICRA. pp. 2913–2920. IEEE (2011)
- Laina, I., Rieke, N., et al.: Concurrent segmentation and localization for tracking of surgical instruments. In: Proc MICCAI. pp. 664–672 (2017)
- Markelj, P., et al.: A review of 3d/2d registration methods for image-guided interventions. MediIA 16(3), 642–661 (2012)
- 8. Murphy, R.J., et al.: Design and kinematic characterization of a surgical manipulator with a focus on treating osteolysis. Robotica **32**(6), 835–850 (2014)
- 9. Otake, Y., et al.: Piecewise-rigid 2d-3d registration for pose estimation of snake-like manipulator using an intraoperative x-ray projection. In: Proc SPIE Med Imag. vol. 9036, p. 90360Q (2014)
- 10. Unberath, M., Zaech, J.N., et al.: Deepdrr a catalyst for machine learning in fluoroscopy-guided procedures. In: Proc MICCAI. Springer (2018)
- Walker, I.D., et al.: Snake-like and continuum robots. In: Springer Handbook of Robotics, pp. 481–498 (2016)